Digital demodulation system for low-coherence interferometric sensors based on highly birefringent fibers

Waclaw Urbanczyk, Magdalena S. Nawrocka, and Wojtek J. Bock

A new type of demodulation system for low-coherence interferometric sensors based on highly birefringent fibers is presented. The optical path delay introduced by the sensor is compensated in four detection channels by quartz crystalline plates of appropriate thickness. The system can be used to decode a single-point sensor with a resolution of 2.5×10^{-3} or two serially multiplexed sensors with decreased resolution. In a multiplexed configuration each sensor is served by two detection channels. By tilting the quartz plates, we can tune the initial phase shift between interference signals in successive channels to differ by $\pi/8$ or $\pi/4$, respectively, for a single-point or a multiplexed configuration. We transferred the sinusoidal intensity changes into digital pulses by appropriate electronic processing, which eventually allows for an unambiguous phase-shift measurement with a resolution of 1/8 or 1/4 of an interference fringe. The system performance for the measurement of hydrostatic pressure changes and simultaneous changes of hydrostatic pressure and temperature is demonstrated. The pressure sensors are based on side-hole fiber to ensure high sensitivity and an operation range of 2.4 MPa. A new configuration for temperature compensation of hydrostatic pressure sensors is proposed, which is better suited for dynamic pressure measurements. In this configuration the sensing and compensating fibers are located in the same compartment of the sensor housing. © 2001 Optical Society of America

OCIS codes: 060.2370, 060.4230, 060.2420, 120.3180.

1. Introduction

In recent years many sensing devices based on the principle of low-coherence interferometry have been developed.[1,2] Such devices are composed of sensing and receiving interferometers arranged in tandem, each having an optical path delay (OPD) greater than the coherence length of the source and almost equal to each other. If these conditions are fulfilled, the differential interference signal can be observed at the output of the receiving interferometer. An attractive feature of the low-coherence methods is that they allow for measurements of both absolute value and relative changes of the measurand affecting the sensing interferometer. The absolute measurements are performed by mechanical[3] or electronic[4,5] scanning of the OPD in the receiving interferometer until it is an exact match with that introduced by the sensing interferometer. An absolute measurement of the OPD can also be realized by use of a spectrum analyzer instead of a receiving interferometer as the decoding device. In this case, the absolute value of the OPD is determined from the spacing of peaks in the spectrum of light that emerges from the sensing interferometer.[6,7]

The demodulation method that we describe also uses a low-coherence interferometric principle. A decoding interferometer is composed of four detection channels that contain crystalline quartz plates to compensate for the OPD introduced by the interrogated sensor. The fading problem, which is the main difficulty in interferometric measurements, is solved when we tilt the quartz plates, thereby introducing an initial phase shift between interference signals and eventually allowing for digital phase measurements with a resolution of 1/8 or 1/4 of an interference fringe, depending on the number of multiplexed sensors. The proposed solution of the fading problem is to some extent similar to that by use of two wavelengths to create interference signals

W. Urbanczyk (urban@rainbow.if.pwr.wroc.pl) and M. S. Nawrocka are with the Institute of Physics, Wroclaw University of Technology, Wybrzeze Wyspianskiego 27, Wroclaw 50-370, Poland. W. J. Bock is with the Laboratoire d'Optoélectronique, Département d'Informatique, Université du Québec à Hull, P.O. Box 1250, Station B, Hull, Québec J8X 3X7, Canada.

shifted in phase by $\pi/2$. Although the two-wavelength techniques have been successfully applied in many practical devices,[8-13] they have two limitations. First, the wavelength difference between detection channels must be tuned individually to ensure the quadrature condition. Second, a dephasing problem arises when the OPD varies significantly from its initial value because of a change in measurand, which ultimately results in the departure of a detection system from a quadrature condition. These main limitations of the two-wavelength method have been overcome to a certain degree by use of three,[14-16] four,[17] or even five[18] wavelengths to interrogate the sensing interferometer. The five-wavelength method in particular brings about a significant reduction in measurement errors that are due to measurand-induced changes in the OPD and relaxes the conditions for phase differences between individual interference signals.

In the proposed detection method the dephasing problem does not appear at all. In contrast to the multiwavelength techniques, the phase differences between detection channels remain the same throughout the entire measurement range. Although the proposed method can be applied to any fiber-optic sensor based on highly birefringent fibers, its performance was tested in hydrostatic pressure and temperature measurements.

It has already been shown that highly birefringent fibers can be used for the measurement of quasi-static changes of pressure, temperature, or elongation.[19-22] However, there is also a need for reliable sensors to measure dynamic pressure changes with a few kilohertz bandwidth. Such sensors could be used in civil engineering to monitor vibrations of bridges, dams, and large buildings with specially developed hydraulic pads integrated with fiber-optic pressure sensors that serve as load-pressure transducers. This technology has already been used successfully to monitor quasi-static loads.[23]

Highly birefringent fibers are sensitive to pressure and temperature, with the result that fiber-optic pressure sensors based on this type of fiber have to be compensated for temperature. Most often a reference fiber located as close as possible to the sensing fiber is used to ensure temperature compensation.[24] However, this method of compensation is not suitable for sensors that are used to measure fast pressure changes, which always induce temperature gradients between the sensing and the reference fibers. Therefore we propose a new sensor configuration based on highly birefringent side-hole fiber, which provides better temperature compensation than already known solutions.

We also tested the sensor configuration that allows for the simultaneous measurement of pressure and temperature changes. As sensing elements we used side-hole and bow-tie fibers spliced together with polarization axes rotation by an angle of 67.5°, which ensures the highest contrast for the interference patterns associated with the bow-tie fiber itself and for
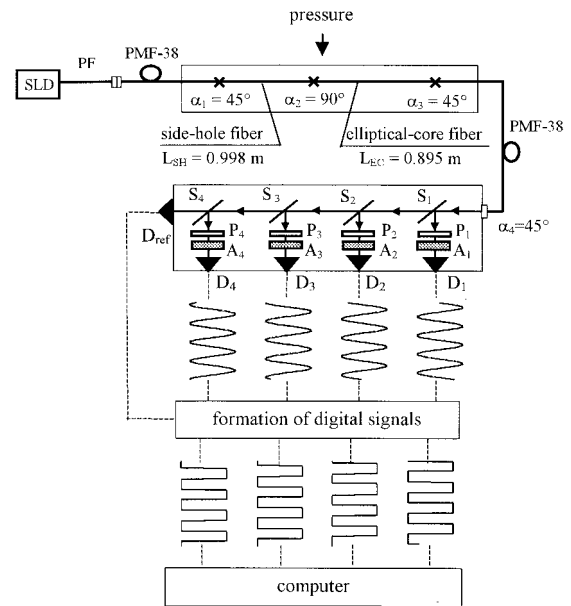

Fig. 1. Scheme of the system with four detection channels for decoding a temperature-compensated pressure sensor: SLD, superluminescent diode; PF, polarizing fiber; PMF-38, highly birefringent fiber from Corning; S_{1-4}, beam splitters, P_{1-4}, quartz delay plates; A_{1-4}, analyzers; D_{1-4}, D_{ref}, photodiodes.

the differential pattern produced by the two fibers. We used the bow-tie fiber as a temperature-sensing element while information about pressure change was decoded from the differential pattern produced by the side-hole fiber and the bow-tie fiber. The sensor characteristics and responses to simultaneous changes in pressure and temperature are demonstrated.

2. Principle of Operation

The system shown in Fig. 1 is powered by a superluminescent diode from Anritsu, Ltd. and pigtailed with 3M polarizing fiber. Linearly polarized light from the polarizing fiber is coupled by a polarization-maintaining connector into one mode of the linking fiber (Corning PMF-38). The linking fiber and the active part of the sensor are spliced to each other with polarization axes rotation of $\alpha_1 = 45°$. Therefore, two polarization modes are excited in the first active element of the sensor. Figure 1 shows the construction of the temperature-compensated sensor for the measurement of pressure changes. The sensor is composed of side-hole and elliptical core fibers that were spliced with polarization axes rotation of $\alpha_2 = 90°$. The differential configuration of the sensor ensures compensation of the temperature effects. The compensating fiber was spliced with a highly birefringent leading-out fiber with polarization axes rotation of $\alpha_3 = 45°$, and the output of the leading-out fiber was aligned by $\alpha_4 = 45°$ with respect to the polarization axes of the quartz delay plates. These rotations ensure the maximum contrast of interference signals in the detection channels.[25-27] The interference phenomenon can be observed in the detection chan-
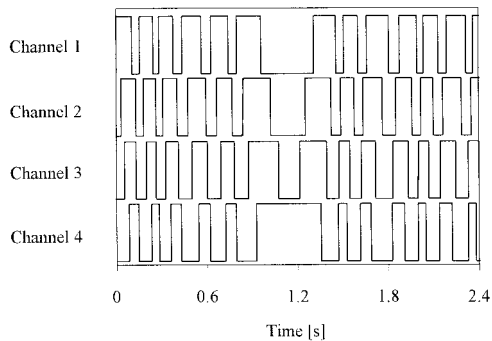
Fig. 2. Response of digital outputs of a four-channel detection unit to increasing and decreasing pressure.

nel only if the total OPD ΔR_S introduced by the sensor is compensated by OPD ΔR_Q introduced by the quartz plates. The detection system is composed of four channels for the registration of interference signals and one channel for the measurement of average intensity at the sensor output. In the system that serves only one sensor, all the plates have the same thickness (4 mm). The plates can be tilted with respect to the incident beam to differentiate the initial phase shift of the interference signal in each decoding channel. The intensity registered in the ith detection channel can be represented by the following equation:

$$I_i = I_0[1 + V_{S/-Q}\gamma(\Delta R_S - \Delta R_Q)\sin(\Delta\phi_S - \Delta\phi_Q{}^i)], \tag{1}$$

where I_0 is the average intensity monitored by the reference detector, γ is a contrast function associated with the source spectrum, and $V_{S/-Q}$ is the contrast at the center of the interference pattern. If the azimuths of all the system elements are such as those shown in Fig. 1, $V_{S/-Q}$ would reach a maximum value equal to 0.5. The phase shifts $\Delta\phi_Q{}^i$ introduced by the quartz plates in successive channels differ by $\pi/4$, which corresponds to 1/8 of an interference fringe. At the same time, the contrast of all the interference signals remains practically the same because γ is a slowly changing function of OPD imbalance ($\Delta R_S - \Delta R_Q$) compared with the fast intensity variations associated with interference fringes. Sinusoidal intensity changes registered in the detection channels are converted into digital signals in such a way that a high level is generated when interference signal I_i is greater than the average intensity I_0 and a low level is generated for $I_i < I_0$. This version of the detection system allows for the measurement of fast phase changes that occur in a sensing interferometer with a resolution of 1/8 of an interference fringe and for easy recognition of the direction of phase changes (see Fig. 2). The counting speed is approximately 10 kHz and is limited by the computer board for data acquisition and the p-i-n photodiodes.

We experimentally determined that for proper operation of the electronic unit that forms digital pulses, the amplitude of the interference signal can-

not be lower than 10% of the average intensity. Therefore, to achieve the highest possible operation range, the initial OPD of sensor $\Delta R_S{}^0$ (at atmospheric pressure) should satisfy the condition $V_{S/-Q}$ $\gamma(\Delta R_S{}^0 - \Delta R_Q) = 0.1$. When the sensor OPD changes with applied pressure, the contrast of the interference signal first increases to a maximum value equal to $V_{S/-Q}$ and then starts to decay until it reaches the critical value on the other side of the pattern envelope, i.e., $V_{S/-Q}$ $\gamma(\Delta R_S{}^0 + \Delta R_S{}^{P_{max}} - \Delta R_Q) = 0.1$, where $\Delta R_S{}^{P_{max}}$ constitutes the system operation range. For the experiments described in this paper we used a superluminescent diode from Anritsu, Ltd. with $\lambda_0 = 849$ nm and $\delta\lambda = 17$ nm, for which we achieved an operation range of $\Delta R_S{}^{P_{max}} = 52\lambda_0$ (approximately 420 counts), which was determined primarily by the spectral width of the light source and by the value of the $V_{S/-Q}$ contrast at the pattern center. Parameter $V_{S/-Q}$ depends on precision of angular alignment of successive sensor elements ($\pm 5°$) (Ref. 25) and on phase retardation uniformity introduced by the quartz plates over the wave-front cross section. To focus all the energy that comes from the sensor output on the p-i-n photodiodes, we used a convergent beam with an aperture angle of approximately $2°$. Because of the variations in crystal birefringence, in effective thickness with incident angle and the changes in orientation of the plane of incidence with respect to the crystal optical axis, the phase retardation for boundary rays differs from that for the central ray by $\pm 4°$ for a 4-mm thick quartz plate. As the photodiodes average intensity over the entire active area, such a retardation nonuniformity decreases the contrast $V_{S/-Q}$. By application of straightforward intensity averaging it can be shown that the drop in contrast is only 2% in this case.

Another possible cause of contrast degradation can be nonuniformity of the quartz plate thickness over the wave-front cross section. The diameter of the beam that passes through the plate is 3 mm. We assume $0.4°$ as an acceptable variation of phase retardation across the beam caused by the change in plate thickness, which is ten times lower than that caused by beam convergence. This value allows us to estimate the tolerance for plate parallelism at ± 6 arc sec, which is a modest requirement.

Technologically, we can control the length of the sensor elements to a precision of ± 2 mm, which corresponds to $\pm\lambda_0$ in terms of retardation. There is no need to control the retardation introduced by the decoding plates to a much higher accuracy. For quartz plates, the thickness variation equivalent to retardation $\pm\lambda_0$ equals ± 0.01 mm at $\lambda_0 = 849$ nm, which can be used to determine the plate thickness tolerance in different detection channels.

3. Hydrostatic Pressure Measurements

The construction of the temperature-compensated sensor for hydrostatic pressure measurements is shown in Fig. 1. The sensing element is composed of side-hole fiber and elliptical-core fiber spliced with

polarization axes rotation of 90°. A high sensitivity to pressure $K_{SH}{}^{P} = -123.5$ rad/MPa m and a low sensitivity to temperature $K_{SH}{}^{T} = -0.78$ rad/K m are characteristics of side-hole fiber.[28] The sensitivity of the elliptical-core fiber to pressure and temperature equals, respectively, $K_{EC}{}^{P} = 0.90$ rad/MPa m and $K_{EC}{}^{T} = -0.87$ rad/K m. The phase shift induced simultaneously by temperature and pressure on the two sensing elements is given by

$$\Delta\phi(T, p) = S^{T}\Delta T + S^{P}\Delta p, \qquad (2)$$

where S^{T} and S^{P} are overall sensitivities to temperature and pressure as represented by the following expressions:

$$S^{T} = K_{SH}{}^{T}L_{SH} - K_{EC}{}^{T}L_{EC}, \qquad (3)$$

$$S^{P} = K_{SH}{}^{P}L_{SH} - K_{EC}{}^{P}L_{EC}. \qquad (4)$$

In Eqs. (3) and (4), L_{EC} and L_{SH} are the lengths of the elliptical-core and side-hole fibers, respectively. To ensure the total temperature compensation of the sensors, the lengths of the side-hole and elliptical-core fibers must be inversely proportional to their sensitivity to temperature:

$$\frac{K_{EC}{}^{T}}{K_{SH}{}^{T}} = \frac{L_{SH}}{L_{EC}}. \qquad (5)$$

One should note that, although the temperature-induced phase shifts in the two fibers are compensated, the pressure-induced phase changes add to each other, because of opposite signs of pressure sensitivity in side-hole and elliptical-core fibers. This specific feature of the side-hole fiber makes it possible to locate the sensing and compensating fibers in the same place on the sensor housing. Such sensor construction is better suited for compensation of temperature effects associated with fast compression and decompression processes than for standard compensation configuration, in which pressure affects only on the sensing elements.[24] Fast pressure changes always cause temperature changes and therefore temperature differences between sensing and compensating elements, if they are located in different places.

Pressure that affects a sensor decreases its total group delay. According to the operating principle of our detection method, the total OPD introduced by the sensor must satisfy the following condition to ensure the maximum operation range:

$$\Delta N_{SH}L_{SH} - \Delta N_{EC}L_{EC} = \Delta N_{Q}d_{Q1} + 0.5\Delta R_{S_{max}}{}^{P}, \qquad (6)$$

where $\Delta N_{EC} = 3.70 \times 10^{-4}$, $\Delta N_{SH} = 3.84 \times 10^{-4}$, and $\Delta N_{Q} = 8.86 \times 10^{-3}$ represent the group birefringence of the elliptical-core fiber, the side-hole fiber, and the quartz plate, respectively, and d_{Q1} represents the plate thickness. For hydrostatic pressure measurements we used plates with a thickness of $d_{Q1} = 4$ mm, which introduced a group delay of approximately $42\lambda_{0}$.

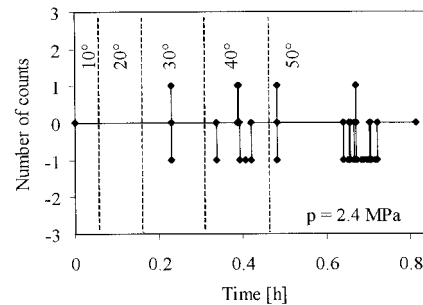Solving Eqs. (5) and (6), we determined the lengths

Fig. 3. Sensor response to temperature at an applied pressure of 2.4 MPa.

of elliptical-core and side-hole fibers to be $L_{EC} = 0.895$ m and $L_{SH} = 0.998$ m. The residual sensitivity of the sensor to temperature S^{T} is limited by the precision of Eq. (5). In practice, lengths L_{EC} and L_{SH} can be controlled to within a tolerance of 2 mm. Substituting this value into Eq. (3) we obtained the technological limit for temperature sensitivity $S^{T} < 2.4 \times 10^{-3}$ rad/K. Such a small residual temperature drift would generate a phase response equivalent to the system resolution equal to 0.785 rad (1/8 of an interference fringe) for temperature changes of approximately 300 °C, a temperature range that is much higher than what is necessary for most technical applications.

The sensing and compensating fibers were wound onto a 7-cm-diameter coil and placed in a steel housing. Such a configuration diminishes the sensor size and makes it more suited for practical applications. Furthermore, as the sensing and compensating fibers from several loops inside the housing, the sensor becomes much more resistant to temperature gradients in comparison with sensing and compensating fibers that are straight.

We investigated sensor performance by conducting several temperature and pressure tests. We tested the sensor temperature stability at different pressures by using a Haake C temperature stabilizer with a precision of 0.1 °C. The sensor did not react to temperature changes from 10 °C to 50 °C at zero pressure even during fast heating, which introduced a temperature gradient of a few degrees across the sensor housing, which is certainly not the maximum temperature gradient that can be accommodated by the sensor. We did not complete the investigation of this problem because it is difficult to control the temperature distribution across the housing.

At a pressure of $p = 2.4$ MPa, the response to temperature was equal to one count, see Fig. 3. This effect was most probably associated with a difference in second-order sensitivities (dependence of temperature sensitivity on pressure)[29,30] in the side-hole and elliptical-core fibers. Therefore, the difference in second-order effects constitutes a real physical limitation of the effectiveness of temperature compensation in such sensors.

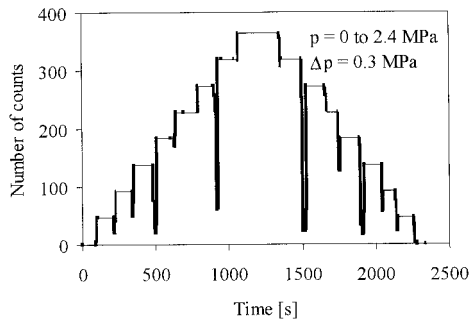We calibrated the system for quasi-static pressure changes by using a Harwood DWT-35 pressure gen-

Fig. 4. Calibration of the sensor for a quasi-static step-type change of pressure in the range from 0 to 2.4 MPa in steps of 0.3 MPa.

erator with a precision of 0.1% as a reference. The calibration results are shown in Fig. 4, where the number of counts registered by a computer (one count corresponding to 1/8 of an interference fringe) are plotted versus applied pressure in the 0–2.4-MPa range in 0.3-MPa steps. The calibration procedure allowed us to determine the sensor's sensitivity to pressure, which is equal to 151.3 counts/MPa (118.8 rad/MPa) and is linear over the entire pressure range that we tested.

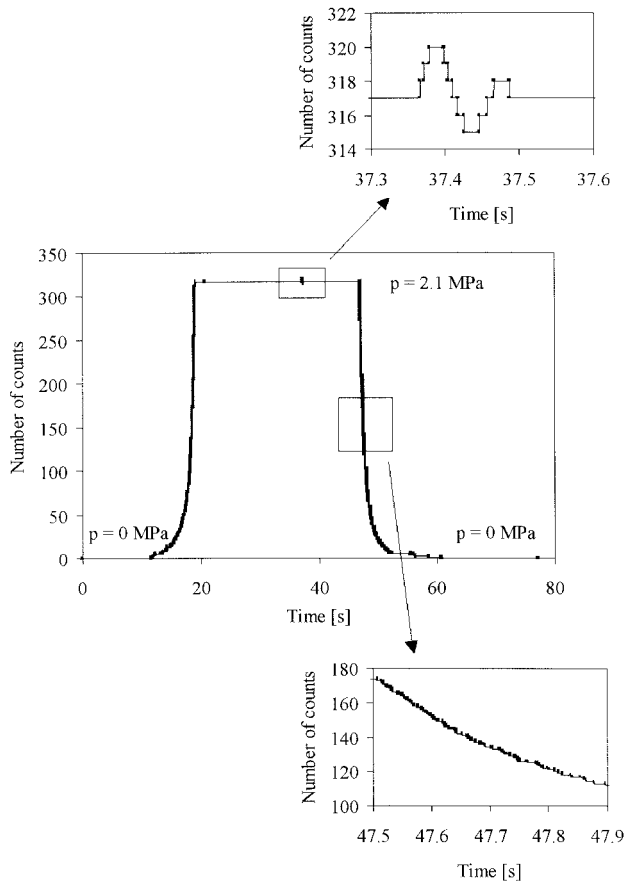Figure 5 shows the response of the sensor to dy-

Fig. 5. Response of the sensor to dynamic pressure changes. Enlarged sections illustrate the time and pressure resolutions of the sensor.
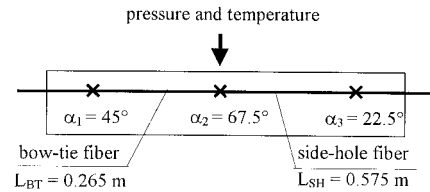

Fig. 6. Construction of a serially multiplexed sensor for simultaneous measurements of pressure and temperature.

namic pressure changes generated in an oil chamber. The enlarged sections illustrate the time and pressure resolution. One count is equivalent to the minimum detectable pressure change equal to 6.6 kPa.

4. Simultaneous Pressure and Temperature Measurements by use of Serially Multiplexed Sensors

The construction of a sensor for simultaneous measurement of pressure and temperature changes is shown in Fig. 6. The active part of the sensor is composed of bow-tie fiber (L_{BT} = 0.265 m) and side-hole fiber (L_{SH} = 0.575 m) spliced with polarization axes rotation of α_2 = 67.5°. In the leading-in fiber only one linearly polarized mode is excited. This fiber is spliced with the first active element of the sensor with polarization axes rotation of α_1 = 45°, which ensures equal excitation of both polarization modes in the first active element of the sensor. The leading-out fiber is spliced to the side-hole fiber with polarization axes rotation of α_3 = 22.5°. The phase changes induced by pressure and temperature are retrieved from two interference patterns. The first is a differential pattern produced by the side-hole and bow-tie fibers whereas the other is produced by the bow-tie fiber itself. Angular alignment of the sensor elements ensures the highest possible theoretical visibility for the two interference patterns $V_{BT/-Q}$ = 0.25 and $V_{SH-BT/-Q}$ = 0.3, respectively.[26,27]

The interference signals associated with the differential pattern are registered in the first two detection channels in which we placed two retardation plates with a thickness of d_{Q1} = 4 mm. By tilting the quartz plates we shifted these two signals in phase by $\pi/2$, which ensures unambiguous fringe counting with a resolution of 1/4 of an interference fringe.

The second interference pattern associated with the bow-tie fiber is monitored in the third and fourth detection channels. To balance the group delay introduced by the bow-tie fiber we placed compensating plates with a thickness of d_{Q2} = 20 mm into these channels and again tilted the plates to introduce a phase shift of $\pi/2$.

High pressure sensitivity of the side-hole fiber causes the differential interference pattern to be much more sensitive to pressure than to temperature. At the same time, the pattern produced by the bow-tie fiber itself is almost equally sensitive to temperature and pressure. We could easily retrieve information about the changes in pressure Δp and temperature ΔT by solving a set of linear equations, if phase shifts $\Delta\phi_{BT}$ (p, T) and $\Delta\phi_{SH-BT}$ (p, T) are
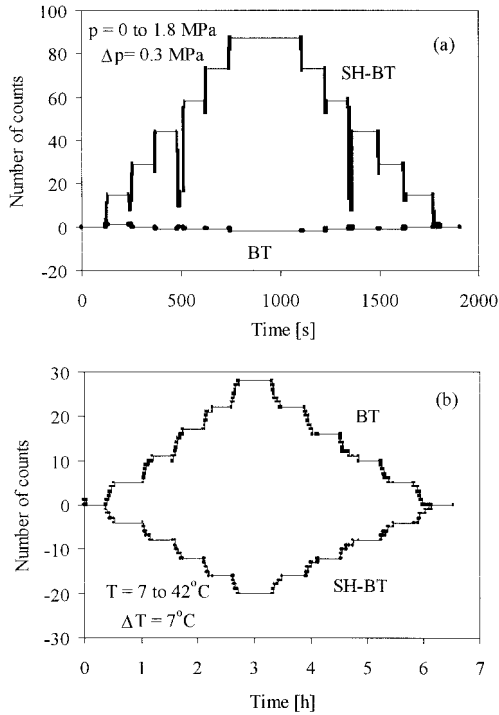
Fig. 7. Calibration of the multiplexed sensor to pressure and temperature. The phase increases in the differential pattern (SH–BT) and the pattern associated with the bow-tie fiber (BT) are linear versus (a) pressure and (b) temperature.

measured simultaneously and sensitivity coefficients to pressure and temperature are known in advance. In respective interference patterns, these coefficients are given by the following relations:

$$S_{BT}{}^{P} = K_{BT}{}^{P} L_{BT}, \qquad (7)$$

$$S_{BT}{}^{T} = K_{BT}{}^{T} L_{BT}, \qquad (8)$$

$$S_{SH-BT}{}^{P} = K_{SH}{}^{P} L_{SH} - K_{BT}{}^{P} L_{BT}, \qquad (9)$$

$$S_{SH-BT}{}^{T} = K_{SH}{}^{T} L_{SH} - K_{BT}{}^{T} L_{BT}. \qquad (10)$$

To determine the sensitivity coefficients we calibrated the system for quasi-static pressure and temperature; see Fig. 7, which shows the number of counts registered by the computer versus applied pressure and temperature. The response of the sensor to pressure and temperature is linear in both detected patterns. By fitting measurement data, we found the coefficients $S_{BT}{}^{P}$, $S_{BT}{}^{T}$, $S_{SH-BT}{}^{P}$, and $S_{SH-BT}{}^{T}$. In the differential pattern the sensitivities are equal to $S_{SH-BT}{}^{P} = 48.18$ counts/MPa (75.64 rad/MPa) and $S_{SH-BT}{}^{T} = -0.568$ counts/K (-0.892 rad/K), respectively. For the pattern produced by the bow-tie fiber the sensitivities are equal to $S_{BT}{}^{P} = -1.329$ counts/MPa (-2.087 rad/MPa) and $S_{BT}{}^{T} = 0.817$ counts/K (1.283 rad/K).

Figure 8(a) shows the response of the sensor to simultaneous step-type changes of pressure and temperature. Knowing the sensitivity coefficients, we could solve the set of linear equations and determine simultaneous changes of the two parameters [Figs.
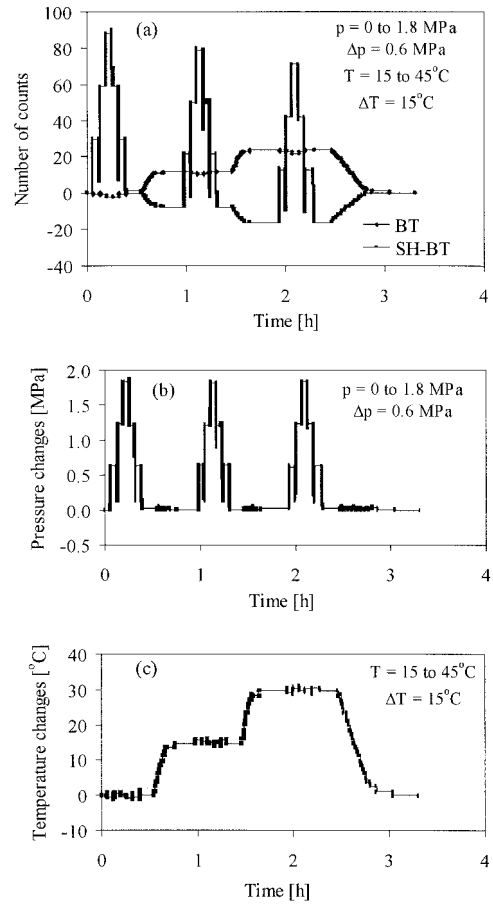

Fig. 8. Response of the multiplexed sensor to simultaneous step-type changes in (a) pressure and temperature in steps of 0.6 MPa and 15 °C, respectively, (b) reconstructed pressure values, (c) temperature.

8(b) and 8(c)]. The maximum difference between reconstructed and actual values of applied pressure and temperature is equal to 0.02 MPa and 1 °C, respectively, which in both cases corresponds to 1% of a sensor's full scale.

5. Summary
We have presented a flexible detection system based on a fringe-counting method for decoding low-coherence interferometric sensors. The performance of the system was tested by measurements of hydrostatic pressure changes with a single temperature-compensated sensor and also by simultaneous measurements of pressure and temperature changes with two serially multiplexed sensors. In both cases the side-hole fiber was used as one of the sensing elements. The unique features of this fiber, such as high sensitivity to pressure and the negative sign of the sensitivity, played an essential role in system performance.

For a temperature-compensated sensor, the negative sign of pressure sensitivity in the side-hole fiber made it possible to locate the sensing and compensating fibers in the same compartment of the sensor head. This prevented temperature gradients be-

tween the two elements and made the sensor almost insensitive to temperature changes. The residual temperature drift of the order of 0.2% of sensor's full scale for temperature change at 40 °C is most probably associated with the second-order effects. Such sensor construction is especially suitable for dynamic measurement, in which the fast compression or decompression always induces temperature changes and could generate false readings if the sensing and compensating elements were located at different places in the sensor head. Optimization of the initial OPD introduced by the sensor ensured a resolution equal to 2.5×10^{-3}, which is limited by the spectral linewidth of the source and precision of the angular alignment of the respective sensor elements. One count of the four-channel decoding unit corresponds to a $\pi/4$ rad phase increase. The operation range of the tested sensor was equal to 2.4 MPa, which could easily be modified if one were to change the lengths L_{SH} and L_{EC} of the two sensing elements and also the thickness of the compensating quartz plate d_{Q1}.

The feasibility of a decoding system for simultaneous pressure and temperature measurements has also been demonstrated. However, for this mode of operation, the resolution of the system is significantly lower. One of the reasons is that only two detection channels are used to decode the phase changes associated with the interference pattern in question. For this configuration one count corresponds to $\pi/2$ rad. Furthermore, for multiplexed systems, the theoretical maximum contrast in both interference patterns is approximately 0.3 whereas for the single-sensor configuration it equals 0.5. Finally, for multiplexed systems the operation range associated with each interference pattern is used to register pressure and temperature changes whereas for single-sensor systems it is assigned only to pressure changes. The effect of these factors is to reduce the resolution of the two parameters in simultaneous measurements to the level of 10^{-2}, which corresponds to 0.02 MPa and 1 °C, respectively, for temperature and pressure readings.

References

1. Y. J. Rao and D. A. Jackson, "Recent progress in fiber optic low-coherence interferometry," Meas. Sci. Technol. **7**, 981–999 (1996).
2. K. T. V. Grattan and B. T. Meggitt, *Optical Fiber Sensor Technology* (Chapman & Hall, London, 1995).
3. T. Bosselmann and R. Ulrich, "High accuracy position-sensing with fiber-coupled white-light interferometers," in *Proceedings of the Second International Conference on Optical Fiber Sensors* (VDE-Verlag GmbH, Berlin-Offenbach, Germany, 1984), pp. 361–364.
4. S. Chen, A. W. Palmer, K. T. C. Grattan, and B. T. Meggitt, "Digital signal-processing techniques for electronically scanned optical-fiber white-light interferometry," Appl. Opt. **31**, 6003–6010 (1992).
5. W. J. Bock, W. Urbanczyk, and M. B. Zaremba, "Electronically scanned white-light interferometric sensor employing highly birefringent fiber," Opt. Commun. **101**, 157–162 (1993).
6. R. Ulrich, "Theory of spectral encoding for fiber-optic sensors," in *Optical Fiber Sensors*, A. N. Chester, S. Martellucci, A. M. Verga Scheggi, eds., NATO ASI Series (Nijhoff, Dordrecht, The Netherlands, 1987), pp. 73–130.
7. M. T. Velluet, P. Graindorge, and H. J. Arditty, "Fiber optic pressure sensor using white-light interferometry," in *Fiber Optic and Laser Sensors V*, R. P. DePaula and E. Udd, eds., Proc. SPIE **838**, 78–83 (1987).
8. R. D. Turner, D. G. Laurin, and R. M. Measures, "Localized dual wavelength fiber-optic polarimeter for the measurement of structural strain and orientation," Appl. Opt. **31**, 2994–3003 (1992).
9. N. Furstenau, M. Schmidt, W. J. Bock, and W. Urbanczyk, "Dynamic pressure sensing with a fiber-optic polarimetric pressure transducer with two-wavelength passive quadrature readout," Appl. Opt. **37**, 663–671 (1998).
10. A. Ezbiri and R. P. Tatam, "Passive signal processing for a miniature Fabry-Perot interferometric sensor with a multi-mode laser diode source," Opt. Lett. **20**, 1818–1820 (1995).
11. A. D. Kersey, M. A. Davis, and M. J. Marrone, "Differential polarimetric fiber-optic sensor configuration with dual wavelength operation," Appl. Opt. **28**, 204–206 (1989).
12. A. D. Kersey, M. Corke, and D. A. Jackson, "Linearised polarimetric optical fiber sensor using a heterodyne-type signal recovery scheme," Electron. Lett. **20**, 209–211 (1984).
13. J. L. Santos, A. P. Leite, and D. A. Jackson, "Optical fiber sensing with a low-finesse Fabry-Perot cavity," Appl. Opt. **31**, 7361–7366 (1992).
14. A. Ezbiri and R. P. Tatam, "Three wavelength passive homodyne signal processing technique for miniature interferometric sensors," in *Interferometry VIII: Techniques and Analysis*, M. Kujawinska, R. J. Pryputniewicz, and M. Takeda, eds., Proc. SPIE **2544**, 177–184 (1995).
15. M. Schmidt, N. Furstenau, W. J. Bock, and W. Urbanczyk, "Fiber-optic polarimetric strain sensor with three-wavelength digital phase demodulation," Opt. Lett. **25**, 1334–1336 (2000).
16. M. Schmidt and N. Furstenau, "Fiber-optic extrinsic Fabry-Perot interferometer sensors with three-wavelength digital phase demodulation," Opt. Lett. **24**, 599–601 (1999).
17. A. Ezbiri and R. P. Tatam, "Interrogation of low finesse optical fibre Fabry-Perot interferometers using a four wavelength technique," Meas. Sci. Technol. **7**, 117–120 (1996).
18. A. Ezbiri and R. P. Tatam, "Five wavelength interrogation technique for miniature fiber optic Fabry-Perot sensors," Opt. Commun. **133**, 62–66 (1997).
19. F. Picherit and J. L. Mineau, "Interferometric-polarimetric force and temperature sensor using high and low birefringence fibers with a short coherence length source," Opt. Commun. **79**, 295–299 (1990).
20. W. J. Bock and T. A. Eftimov, "Simultaneous hydrostatic pressure and temperature measurement employing an LP_{01}–LP_{11} fiber-optic polarization-sensitive intermodal interferometer," IEEE Trans. Instrum. Meas. **43**, 337–340 (1994).
21. W. J. Bock and W. Urbanczyk, "Temperature desensitization of a fiber-optic pressure sensor by simultaneous measurement of pressure and temperature," Appl. Opt. **37**, 3897–3901 (1998).
22. M. P. Varnham, A. J. Barlow, D. N. Payne, and K. Okamoto, "Polarimetric strain gauges using high birefringent fibers," Electron. Lett. **19**, 699–700 (1983).
23. W. J. Bock, W. Urbanczyk, T. A. Eftimov, and J. Chen, "Development and performance of fiber optic sensor systems for absolute and quasi-static measurements in civil engineering

applications," in *Proceedings of the International Conference on Applications of Photonic Technology*, G. A. Lampropoulos and R. A. Lessard, eds. (Plenum, New York, 1997), pp. 723–729.

24. J. P. Dakin and C. A. Wade, "Compensated polarimetric sensor using polarization-maintaining fibre in a differential configuration," Electron. Lett. **20,** 51–53 (1984).

25. W. Urbanczyk, P. Kurzynowski, A. W. Wozniak, and W. J. Bock, "Contrast analysis for tandem of white-light fiber-optic interferometers," Opt. Commun. **135,** 1–6 (1997).

26. A. W. Wozniak, P. Kurzynowski, W. Urbanczyk, and W. J. Bock, "Contrast analysis for fiber-optic white-light interferometric system," Appl. Opt. **36,** 8862–8870 (1997).

27. W. Urbanczyk and W. J. Bock, "Visibility of white-light interference patterns for chain of coherence multiplexed sensors based on highly birefringent fibers," Opt. Eng. **32,** 2100–2105 (1993).

28. W. J. Bock, W. Urbanczyk, and J. Wójcik, "Characterization of elliptical-core side-hole fibers for interferometric pressure sensing," in *Interferometry 94: Interferometric Fiber Sensing*, E. Udd and R. P. Tatam, eds., Proc. SPIE **2341,** 152–159 (1994).

29. W. J. Bock, W. Urbanczyk, R. Buczynski, and A. W. Domanski, "Cross-sensitivity effect in temperature compensated sensors based on highly birefringent fibers," Appl. Opt. **33,** 6078–6083 (1994).

30. W. J. Bock and W. Urbanczyk, "Temperature-hydrostatic pressure cross-sensitivity effect in elliptical core highly birefringent fibers," Appl. Opt. **35,** 6267–6270 (1996).